Int. J. Electrochem. Sci., 15 **(2020)** 4953 – 4963, doi: 10.20964/2020.06.34

International Journal of
ELECTROCHEMICAL
SCIENCE
www.electrochemsci.org

Iridium Surface Treatment by Glow Plasma Treatment and Its Application as Electrocatalyst for Methanol and CO Oxidation

Yao Liang[1], *Hongzhong Cai* [2], *Jiushuai Deng*[3], *Yiqi Cui*[3,*]

[1] City College, Kunming University of Science and Technology, Kunming 650093, China
[2] State Key Laboratory of Advanced Technologies for Comprehensive Utilization of Platinum Metals, Kunming Insitute of Precious Metals, Kunming 650106, China
[3] Faculty of Land Resource Engineering, Kunming University of Science and Technology, Kunming 650093, China
[*]E-mail: kmust_cyq@163.com

Received: 8 February 2020 / *Accepted:* 19 March 2020 / *Published:* 10 May 2020

The regulation of the electrocatalytic activity of an iridium surface using a plasma activation treatment process has been studied experimentally and using first-principles calculations. The microstructures and catalytic properties were investigated using scanning electron microscopy, X-ray diffraction, X-ray photoelectron spectroscopy, cyclic voltammetry and CO-stripping voltammograms. The results show that the plasma activation treatment process can promote the surface energy of iridium particles, thereby increasing their surface activity as a catalyst. Furthermore, the current density of Ir/C-Plasma is 1.46 times higher than that of Ir/C, indicating that the electrocatalytic activity is significantly increased upon increasing the number of surface-active sites. More importantly, the mechanism of the surface activity sites that improves the catalyst performance of the iridium surface was illustrated using first-principle calculations. We also find that CH_3OH molecules form chemical bonds with the dangling bonds localized on the iridium atoms around the vacancies and that these sites have the lowest adsorption energy (–0.578 eV). Meanwhile, the TS results indicate that the dissociation of CH_3OH on a non-vacancy surface was more difficult than on the one-vacancy surface. In addition, the charge transfer further confirms that the vacancies on the iridium surface can provide a large number of active sites for chemical adsorption/desorption, which can promote CO anti-poisoning processes. This study not only reveals the CH_3OH adsorption/desorption reaction mechanism of Ir/C-Plasma, but also provides effective guidance toward improving the catalyst performance of noble metal catalysts.

Keywords: Electrocatalytic activity, iridium surface, first-principles calculations.

1. INTRODUCTION

Hydrogen-oxygen fuel cells may be an important potential source of clean energy in the future due to their high energy density, high power and environment-friendliness [1, 2]. However, the anode

and cathode catalysts used for hydrogen-oxygen fuel cells depend heavily on Pt, which limits the large-scale application of this technology. In recent years, intensive efforts have been devoted to the development of non-platinum-based catalysts [3-5]. Among them, iridium-based catalysts have attracted a significant amount of attention due to their overpotential values being close to zero and high reaction rate [6, 7]. However, the catalytic performance of iridium-based catalysts is not enough to achieve rapid hydrogen production [8]. Therefore, it is desirable to explore a new strategies to improve the performance of iridium-based catalysts.

Previous research has shown that the surface morphology of a catalyst can play a key role in determining its activity, selectivity, and stability [9, 10]. Chen et al. [11] have reported the dependence of the catalytic activity of TiO_2 nanocrystals on their surface facets, which indicated that the catalytic activity mainly originates from a defect-rich surface of TiO_2 {001} and TiO_2 {101}. Mistry et al. [12] have reported that plasma treatment is a powerful method to create defects or embed atoms, which can improve a materials reactivity. These research studies indicate that enhancing the active sites is a key issue to improve the selectivity of a catalyst. It is more difficult to reveal the mechanism of the active sites on the iridium surface due to the many technical difficulties found when observing the active sites on a lattice scale [13].

Fortunately, the development of high performance computer simulations provides a new way to solve the above-mentioned problems. In this work, an Ir/C catalyst was treated using glow plasma, and the microstructure and phase composition of the samples were investigated using scanning electron microscopy, X-ray diffraction and X-ray photoelectron spectroscopy. The catalytic properties of the samples were studied using cyclic voltammetry and CO-stripping voltammograms. Meanwhile, the mechanism of the surface active sites that improves the catalyst performance of the iridium surface was illustrated using first-principle calculations.

2. EXPERIMENTAL AND COMPUTATIONAL DETAILS

2.1 Materials and preparation

The materials used in this experiment including iridium chloride ($IrCl_3$, 99.99% metals basis, Ir ≥63.9%), activated charcoal, sodium perchlorate ($NaClO_4$, 99%) and 5 wt.% Nafion solution were purchased from Aladdin (Shanghai, China).

The preparation of Ir/C was as follows: a) 60 mg of activated charcoal was added to 10 mL of water; b) An ethanol solution of $IrCl_3$ (4 mL, 0.03 mol/L) was added to the solution of activated charcoal; c) The resulting suspension was dispersed using ultrasonication for 30 min and stirred for 4 h using NaOH to adjust the pH to 8–9; d) 2 mL of a 0.85 mol/L aqueous solution of $NaBH_4$ was slowly added to the suspension with stirring, sonicated for 4 h, and stirred for 4 h; e) The suspension was washed with water, filtered, and dried under vacuum at 55 °C for 12 h to give the Ir/C catalyst.

In addition, the Ir/C catalyst was treated with glow plasma using argon as the carrier gas. The working pressure was stabilized at 30–90 Pa, the cathode voltage was 600 V, and the source voltage was 1000 V. After the experiment, the sample were treated at 300 °C for 30 min and then cooled to room temperature in the furnace. The resulting product was named Ir/C-Plasma.

A schematic representation of the glow plasma treatment process is shown in Figure 1. Glow discharge forms a plasma field by applying a voltage between two electrodes. In the plasma field, free electrons and ions are excited and carry sufficient energy. When the plasma bombards the surface of the spherical iridium powder, the iridium atoms on the surface are excited by the high-speed Ar atoms and form surface active sites (e.g. mono-vacancies and di-vacancies), which alters the catalytic performance of the iridium surface.

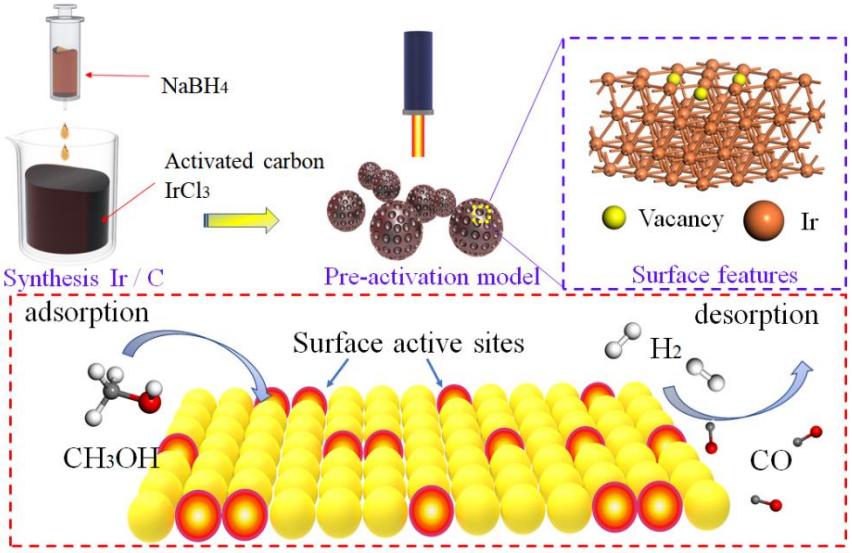

Figure 1. A schematic representation of the glow plasma treatment process.

2.2 The microstructure and phase composition

The microstructure of Ir/C was investigated using scanning electron microscopy (SEM) performed on a Philips 505 (Eindhoven, NL) instrument. The crystalline structures and chemical compositions were analyzed using powder X-ray diffraction (XRD, Rigaku MiniFlex II) using Cu-Kα radiation (λ = 1.541 Å). The scanning rate was 0.5°/s and the 2θ range was 10–90°. The chemical states on the surface of the product was analyzed using X-ray photoelectron spectroscopy (XPS, PHI5000 Versaprobe-II ULVACPHI) employing Al-Kα radiation.

2.3 Preparation of the working electrode

The working electrode was prepared using a literature procedure. Typically, the catalyst dispersion was prepared by mixing 8 mg of the catalyst in 2.5 mL of a solution containing 2.4 mL of ethanol and 100 µL of 5 wt.% Nafion solution followed by ultrasonication for 30 min. A glassy carbon (GC) disk electrode (5 mm in diameter) serves as the support. Prior to use, the GC electrode was polished using an aqueous alumina suspension on a felt polishing pad. The catalyst suspension was transferred using a micropipette onto the GC surface, leading to a catalyst loading of ~0.2 mg/cm^2. The working electrode was dried under a flow of N_2 at room temperature.

2.4 Electrochemical tests

The electrochemical performance was assessed on an electrochemical workstation (CHI760E) using a three-electrode system consisting of a GC electrode, Pt plate counter electrode, and saturated calomel electrode (SCE), which is separated from the working electrode compartment by a closed electrolyte bridge.

The catalyst performance in the room temperature methanol oxidation reaction (MOR) was also measured using cyclic voltammetry. A potential window of 0 V to 1.5 V at a scan rate of 100 $mV \cdot s^{-1}$ was used until a stable response was obtained prior to recording the voltammograms. The electrolyte was 0.1 mol L^{-1} $HClO_4$ with a 2.0 mol L^{-1} CH_3OH aqueous solution. For each catalyst, the current density was normalized by its ECSA to obtain the specific activity. The electrolyte solutions were purged with high-purity N_2 gas for 30 min to reduce the level of dissolved oxygen prior to each cyclic voltammetry measurement and the solution was maintained under a flow of N_2 gas.

The CO dissolution experiment is an important method to study the anti-CO poisoning ability of the catalyst. In the case of the CO-stripping experiment, the working electrode was inserted into the electrolytic cell containing 0.1 mol L^{-1} $HClO_4$ solution as the electrolyte, a carbon rod counter electrode and SCE reference electrode. CO (99.99%) adsorption was conducted at 0.11 V in a CO saturated 0.1 mol L^{-1} $HClO_4$ solution for 15 min and subsequently purged with N_2 (99.999%) for 30 min to remove the dissolved CO from the solution, followed by scanning between 0 and 1.5 V at a scan rate of 100 $mV \cdot s^{-1}$.

2.5 Computational methods

Our first-principles calculations based on density functional theory (DFT) were accomplished by utilizing the Vienna ab initio simulation package (VASP) [15]. The core-valence interaction was depicted by adopting the projector augmented wave method [16]. The exchange-correlation functional used the general gradient approximation (GGA) in the Perdew–Burke–Ernzerhof (PBE) form [17]. The reciprocal space was sampled using the Monkhorst–Pack method [18] of at least 8×8×1 k-points in the Brillouin zone. The kinetic energy cut-off was set at 400 eV and the geometry was optimized until the residual forces and energy were −0.01 eV/Å and 10^{-6} eV/cell, respectively.

According to a previous study [19], a super cell (3×3) five layer Ir (111) slab was modeled with a vacuum thickness of at least 15 Å. In the calculation, the bottom two metal layers were fixed as their bulk truncated structure. The van der Waals (vDW) interaction with a DFT-D3 correction of Grimme [20] was considered in all our calculations. The climbing-image nudged elastic band (CI-NEB) method [21] was used to compute the energy barrier of CH_3OH on the surface. Bader charge analysis was employed to obtain a quantitative description of the anti-CO poisoning ability of the Ir/C-Plasma catalyst [22].

3. RESULTS AND DISCUSSION

3.1 Structure and phase of the iridium catalysts

Figure 2a and 2b display the microstructure and grain distribution of the Ir/C and Ir/C-Plasma catalysts. The morphologies of the samples are nearly spherical with uniform particle sizes. In general, a smaller nanoparticle size exhibits good chemical activity. The particle size of Ir/C and Ir/C-Plasma was 1.98 and 1.92 nm, respectively. This indicates that the Ir/C and Ir/C-Plasma catalysts have good chemical activity [23,24].

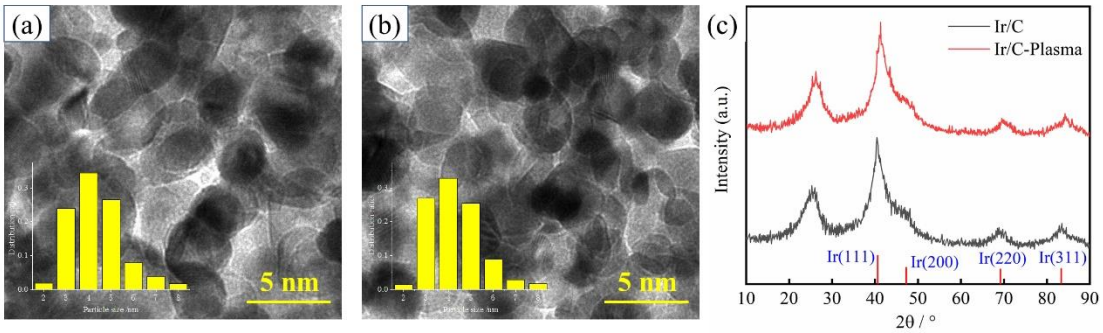

Figure 2. The microstructures and XRD patterns of the samples. TEM image and particle size distribution of (a) Ir/C and (b) Ir/C-Plasma. (c) XRD patterns obtained for Ir/C and Ir/C-Plasma.

Figure 2c displays the XRD patterns of the Ir/C and Ir/C-Plasma catalysts. The 2θ scan data obtained for the films exhibit strong peaks at 2θ = 40.86°, 47.46°, 69.34°, 83.68°, and 88.14° respectively, corresponding to the (111), (200), (220) and (311) peaks of iridium. When compared to Ir/C, the (111) and (200) peaks of Ir/C-Plasma are slightly shifts to a higher diffraction angle. This shift in the diffraction peaks of the sample indicates a decrease in the lattice constant due to an increase in the surface residual stress [25]. The results indicate that the plasma-treatment process is responsible for an increase in the surface energy.

XPS was used to gain a deeper insight into the chemical composition of Ir/C and Ir/C-Plasma, as shown in Figure 3. It can be inferred that the nanoparticles are composed of Ir and C. In Figure 3a, the nanoparticles are primarily composed of Ir and C. The binding energy was corrected based on the C1s peak observed at ~284.5 eV as a standard for the internal binding energy [26]. Notably, the Ir 4f peak was comprised of multiple pairs of overlapping peaks, which can be attributed to the binding energy of Ir $4f_{7/2}$ and Ir $4f_{5/2}$ of the Ir metal species. The other two pairs of peaks correspond to the Ir^{4+} species. The appearance of some Ir^{4+} may be attributed to incompletely restoration during the co-restore reaction. Importantly, the Ir 4f binding energy of the Ir/C-Plasma catalyst was blue-shifted when compared to Ir/C. The positions of the Ir $4f_{7/2}$ peak were 62.09 and 61.93 eV for Ir/C and Ir/C-Plasma, respectively [27]. This was attributed to the surface state of Ir being affected by the glow plasma treatment, which causes lattice compression strain on the Ir surface to cause the blue shift in the Ir 4f binding energy, thereby improving the catalytic activity of the catalyst [28]. It should be noted that the binding energy is strongly correlated with the adsorption/desorption capability of the catalyst surface toward the reaction species.

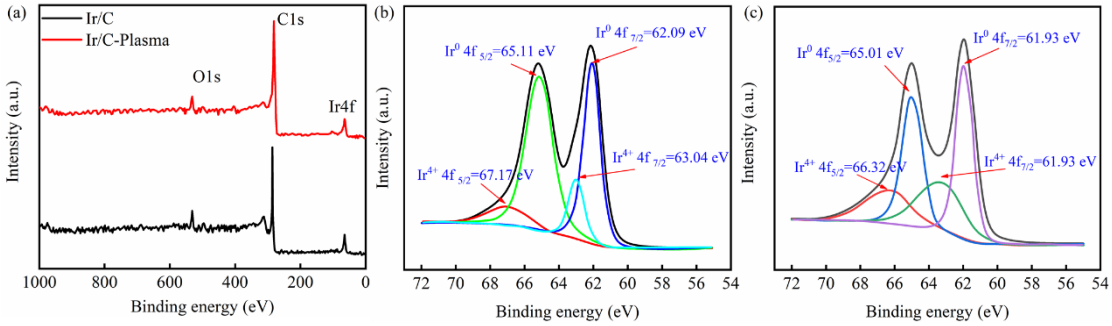

Figure 3. X-ray photoelectron spectroscopy (XPS) results obtained for the samples: (a) Survey spectrum, (b) narrow scan spectrum of Ir/C and (c) narrow scan spectrum of Ir/C-Plasma.

3.2 Electrocatalytic activity of the anode in the methanol oxidation reaction

The catalyst performance during the methanol oxidation reaction (MOR) was also measured using cyclic voltammetry using a 0.1 mol L^{-1} $HClO_4$ with 2.0 mol L^{-1} CH_3OH aqueous solution and the results shown in Figure 4a and Table 1. The literature shows that the higher cathodic peak current density can be used to evaluate the catalytic activity and their comparable peak current densities imply good electrocatalytic activity [29]. According to Figure 4a and Table 1, the current densities (j_m) in the MOR using Ir/C and Ir/C-Plasma were 304.97 and 445.02 mA/mg, respectively and the specific activity (j_s) of Ir/C-Plasma was 1.17 times higher than that observed for Ir/C. This means that Ir/C-Plasma exhibits higher catalytic activity than Ir/C. More significantly, the catalytic performance of Ir/C-Plasma was better than that observed with similar products (Ir-S/C and Pt-Ru/C). One interpretation of this result is that the glow plasma treatment process can produce surface residual stress and active sites on the iridium surface and as a result, the electrocatalytic activity increases strongly upon increasing the number of surface active sites (e.g. vacancies).

Table 1. A summary of the electrochemical parameters obtained for the catalysts.

Sample	j_m (mA·mg^{-1})	S_{ESA} (m^2g^{-1})	j_s (mA·cm^{-2})
Ir/C	304.97	25.4	11.25
Ir/C-Plasma	445.02	35.27	13.21
Ir-S/C[30]	350.82	29.3	12.15
Pt-Ru/C[31]	330.76	28.4	12.58

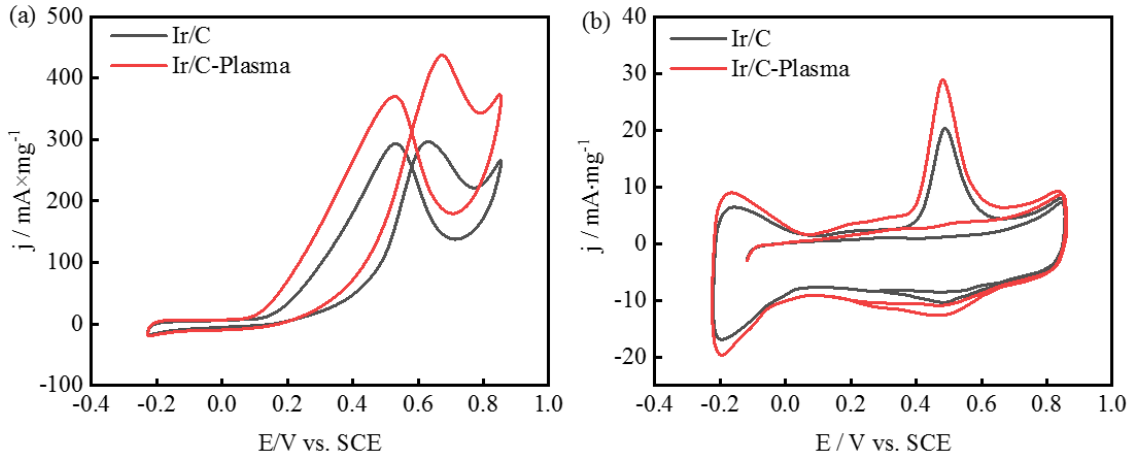

Figure 4. (a) The CV curves obtained for all the catalysts recorded in a 0.1 mol L^{-1} $HClO_4$ with 2.0 mol L^{-1} CH_3OH aqueous solutions solution at 25 °C and a scan rate of 100 mV·s^{-1}. (b) The CO-stripping voltammograms obtained for all the catalysts recorded in a 0.1 mol L^{-1} $HClO_4$ solution at a scan rate of 100 mV·s^{-1}.

The catalysts resistance to CO poisoning during the MOR was evaluated using CO-stripping measurements conducted in a 0.1 mol L^{-1} $HClO_4$ aqueous solution at a scan rate of 100 mV·s^{-1}. Figure 4b shows the electrochemical surface area (S_{ESA}) of the catalysts, which is also summarized in Table 1. The S_{ESA} of Ir/C-Plasma, Ir/C, Ir-S/C and Pt-Ru/C are 35.27, 25.4, 29.3 and 28.4 m^2g^{-1}, respectively. Clearly, Ir/C-Plasma has the largest ESA, which was 1.27, 1.20 and 1.24 times larger than those observed for Ir/C, Ir-S/C and Pt-Ru/C. This implies Ir/C-Plasma has the most active sites on its surface, further showing that the glow plasma treatment process facilitates the catalytic activity through the improved Ir surface structure. The active sites promote the dissociation of CH_3OH and generates more hydroxyl groups on the iridium surface, which can promote the oxidation of CO molecules [32]. Importantly, the onset potential of CO oxidation on Ir/C-Plasma was also the most negative and thus, the glow plasma treatment process has a promotive effect in removing the adsorbed CO on the iridium surface[33].

3.3 Surface activation mechanism

To explore the surface activation mechanism of Ir/C, we investigated the adsorption ability of CH_3OH on the Ir(111) surface. An Ir atom on the surface of the catalyst was replaced by a vacancy and used to represent Ir/C-Plasma. Two kinds of adsorption sites in the Ir(111) plane before the plasma-treatment step are presented in Figure 5. During the relaxation process, the adsorption to other sites is followed by spontaneous migration to the sites shown in Figure 5a and 5b, so we have only considered these type sites. This adsorption energy is defined as follows [34]:

$$E_{adsor} = E_{total} - E_{surface} - E_{CH_3OH} \quad (1)$$

where E_{adsor} is the adsorption energy and $E_{surface}$ and E_{total} are the energies of the Ir(111) surface before and after NO insertion, respectively. E_{CH_3OH} is the energy of an CH_3OH molecule. The calculated negative values obtained for E_{adsor} indicate the preferential adsorption of CH_3OH on the Ir(111) surface.

The adsorption energies obtained for Ir/C and Ir/C-Plasma are –0.302 and –0.578 eV, respectively. It is notable that the Ir/C-Plasma surface has a lower adsorption energy, which provides direct evidence for the formation of chemical bonds between the CH_3OH molecules and dangling bonds localized on the Ir atoms around the vacancies. In addition, the active sites in Ir/C-Plasma have a more-negative adsorption energy when compared the Ir/C, which indicates that the iridium vacancies on the surface offers more attachment points and results in more active sites for CH_3OH absorption.

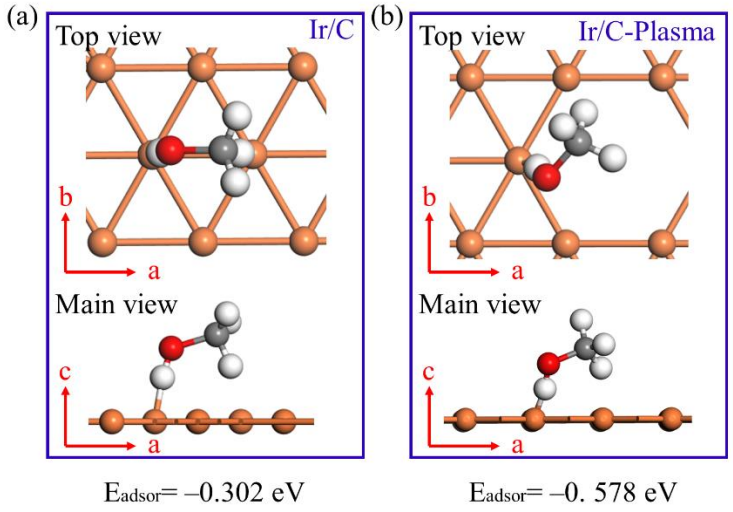

Figure 5. The adsorption structure of CH_3OH on (a) Ir/C and (b) Ir/C-Plasma. The red, grey and white atoms represent O, C and H, respectively; the orange atoms represent Ir.

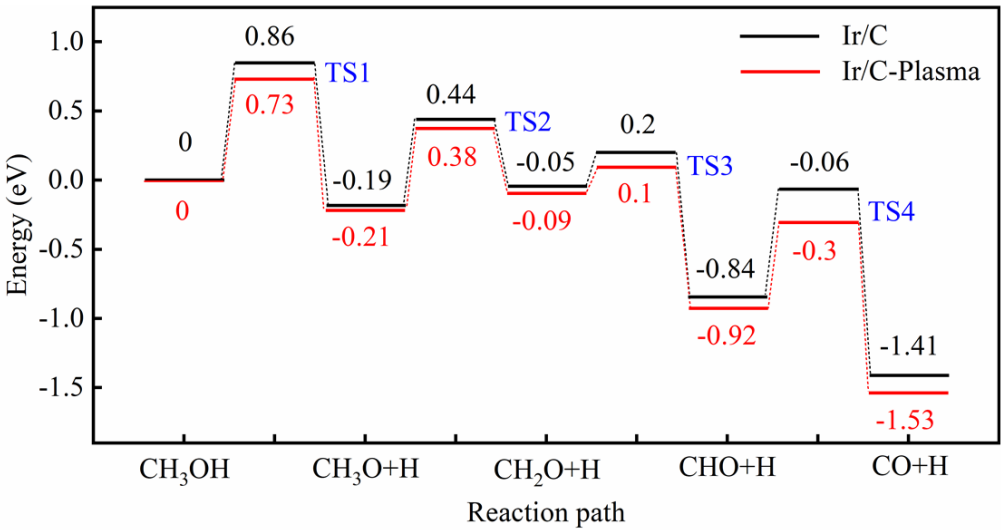

Figure 6. The calculated transition state geometries obtained for the NO → N + O reaction on the Ir(111) surface.

According to the adsorption sites analysis, the O atom-connected H atom was initially adsorbed on the Ir surface. Therefore, the methanol decomposition reaction is shown below:

$$\begin{aligned} &R1: CH_3OH \rightarrow CH_3O+H \\ &R2: CH_3O \rightarrow CH_2O+H \\ &R3: CH_2O \rightarrow CHO+H \\ &R4: CHO \rightarrow CO+H \end{aligned} \quad (2)$$

Furthermore, the transition states for the decomposition of methanol are shown in Figure 6. The reaction barrier (E_{TS}) was defined as the migration energy between the initial state. The results show that the iridium structure before and after plasma treatment are good catalysts for the MOR. Furthermore, when comparing the non-vacancy and one-vacancy Ir(111) surface, it was found that the dissociation of methanol on the no-vacancy surface was more difficult than that observed on the one-vacancy surface. Therefore, the one-vacancy Ir (111) surface has high activity, which leads to the facile MOR to form CO and H. This result is in agreement with the results of the electrocatalytic activity experiments.

For a deeper understanding of the anti-poisoning ability of Ir/C-Plasma, we calculated the charge density difference of the most stable adsorption structure using the following formula: $\rho(r) = \rho_{adsorption}(r) - \rho_{surface}(r) - \rho_{CO}(r)$, where $\rho_{adsorption}(r)$, $\rho_{surface}(r)$ and $\rho_{CO}(r)$ are the charge densities of CO adsorbed on the Ir (111) surface, CO molecule, and clean Ir (111) surface, respectively. Figure 7a shows the electrons are mainly accumulated around the more electronegative CO molecule, as expected for the one-vacancy Ir surface (Figure 7b), albeit with the accumulation of charge density on the CO molecule on the one-vacancy surface being noticeably lower than that observed on the no-vacancy surface.

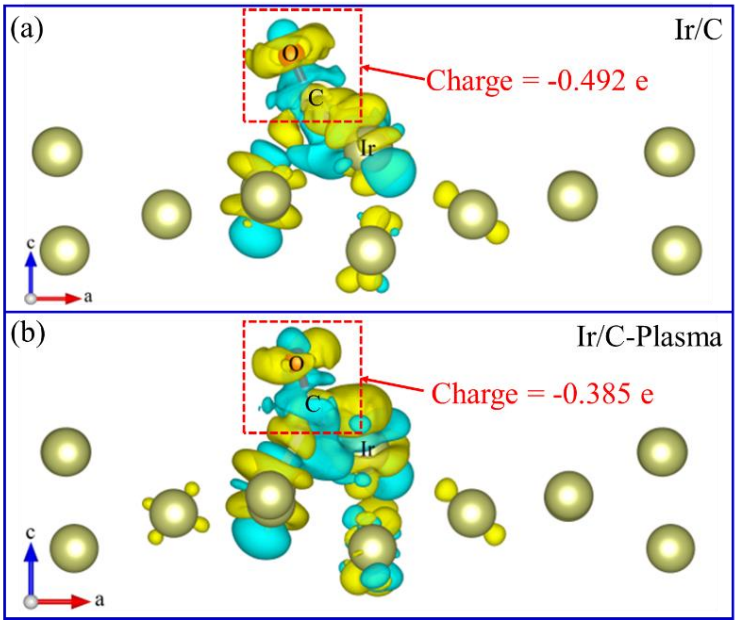

Figure 7. Charge density differences observed for the CO adsorption configurations on the Ir(111) surfaces: (a) Ir/C and (b) Ir/C-Plasma.

The charge transferred to the Ir/C structures was investigated using Bader charge analysis. The results show that charge transfer from the one-vacancy surface to the CO molecule is 0.385 |e|, which is 27.8% lower than that observed for the no-vacancy surface (0.492 |e|). Such a difference in the charge transferred indicates that the surface iridium vacancies can provide a large number of active sites for chemical adsorption/desorption, which can promote the CO anti-poisoning processes.

4. CONCLUSIONS

In summary, the catalytic performance of an iridium surface in the MOR using surface reactive sites control has been studied experimentally and using first-principles calculations. We have found that the particle size of Ir/C and Ir/C-Plasma was 1.98 and 1.92 nm, respectively, which confirmed that the plasma activation treatment could promote the surface energy of the iridium particles, thereby increasing the surface activity as a catalyst. This conclusion was strongly supported by the shift observed in the X-ray diffraction peaks after the plasma activation treatment process. The catalytic behavior results show that the current densities in the MOR observed for Ir/C and Ir/C-Plasma were 304.97 and 445.02 mA/mg. Meanwhile, the electrochemically active area of Ir/C-Plasma was 35.27 $mA \cdot mg_{Pt}^{-1}$, which is 1.27 times higher than the electrochemical active area of the Ir/C catalyst, indicating that the plasma treatment process can improve the anti-poisoning ability of the catalyst. We have also found that the formation of chemical bonds between the CH_3OH molecules and dangling bonds localized on the iridium atoms around the vacancies. Meanwhile, the TS results indicate that CH_3OH dissociation on the no-vacancy surface was more difficult than that observed on the one-vacancy surface. Importantly, the charge transferred gave further evidence that the surface Iridium vacancies provide a large number of active sites for chemical adsorption/desorption, which can promote the selective CO adsorption and degradation process. Our work has used experimental and quantum chemical computational methods to elucidate the CH_3OH adsorption/desorption reaction mechanism, further utilizing it to explain the mechanism of surface activation. In addition, it can provide effective guidance toward controlling the catalyst performance of noble metal catalysts.

ACKNOWLEDGEMENTS
This work was supported financially by the National Nature Science Foundations of China (grant Nos. 51661014, 51664028), the Natural Science Foundation of Yunnan Province, China (grant Nos. 2016FA053), genetic engineering of rare and precious metal materials in Yunnan Province (phase I, 2019) (grant Nos. 2019ZE001)) and open fund supported by State Key Laboratory of New Technology for Comprehensive Utilization of Rare and Precious Metals, China(grant Nos. SKL-SPM-2018015).

References

1. E. Boyle, *Science,* 356 (2017) 700.
2. R. A. Perry and D. L. Siebers, *Nature,* 324 (1986) 657.
3. Munaiah. Y, Boopathi. S, Kumar. S. S and Ragupathy. P, *Mater. Lett*., 239（2019） 184.
4. K. Qi, J. L. Xie and H. Hu, *Chem. Eng. J.*, 352 (2018) 39.

5. X. Cheng, M. Zhang and P. Sun, *Green Chem.*, 18 (2016) 5305.
6. M. A. Goula, N. D. Charisiou and K. N. Papageridis, *J. Environ. Chem. Eng.*, 4 (2016) 1629.
7. A. A. Esparza, R. E. Ferguson and A. Choudhuri. Shafirovich, *Combust. Flame,* 193 (2018) 417.
8. B. Liu, D. Yao, F. Wu and X. Wang, *Ind. Eng. Chem. Res.*, 58 (2019) 20516.
9. S. Taylor, E. Fabbri, P. Levecque, T. J. Schmidt and O. Conrad, *Electrocatalysis-us,* 7 (2016) 287.
10. N. Kamiuchi, K. Sun, R. Aso, M. Tane, T. Tamaoka, H. Yoshida and S. Takeda, *Nat. Commun.*, 9 (2018) 1.
11. S. Chen, A. M. Abdel. Mageed, D. Li, J. Bansmann, S. Cisneros and J. Biskupek, *Angew. Chem. Int. Edit.*, 58 (2019) 10732.
12. H. Mistry, A. S. Varela, C. S. Bonifacio, L. Zegkinoglou and I. Sinev, *Nat. Commun.*, 7 (2016) 12123.
13. J. Feng, C. Zhang, D. Zhou, Z. Xu, D. Morgan and P. M. Voyles, *Microsc. Microanal.*, 23 (2017) 418.
14. J. Zhang, X. Yao, Q. Shao, B. Xu, X. Liang and C. Long, *J. Phys. Chem. C.,* 123 (2019) 16721.
15. G. Kresse, J. Furthmüller, Vienna ab-initio simulation package, 2001, Vienna: Vienna University.
16. P. E. Blöchl, *Phys. Rev. B.,* 50 (1994) 17953.
17. J. P. Perdew, K. Burke and M. Ernzerhof, *Phys. Rev. Lett.*, 77 (1996) 3865.
18. H. J. Monkhorst and J. D. Pack, *Phys. Rev. B.,* 13 (1976) 5188.
19. Z. P. Liu, S. J. Jenkins and D. A. King, *J. Am. Chem. Soc.*, 125 (2003) 14660.
20. O. A. Vydrov and T. V. Voorhis, *J. Chem. Phys.*, 133 (2010) 244103.
21. G. Henkelman, B. P. Uberuaga and H. Jónsson, *J. Chem. Phys.*, 113 (2000) 9901.
22. G. Henkelman, A. Arnaldsson and H. Jónsson, *Comput. Mater. Sci.*, 36 (2006) 354.
23. S.J. Zaidi, M. Bello, A. Al-Ahmed, A.B. Yousaf and M. Imran, *J. Electroanal. Chem.*, 794 (2017) 4.
24. H.L. Xin, S. Alayoglu, R. Tao, A. Genc, C.M. Wang and L. Kovarik, *Nano lett.*, 14 (2014) 6.
25. Q. Luo and A. H. Jones, *Surf. Coat. Tech.*, 205 (2010) 1403.
26. A.P. Dementjev, A. DeGraaf, M.C.M. Sanden, K.I. Maslakov and A.V. Naumkin*, Relat. Mater.*, 9 (2000) 11.
27. A.S. Arico, A.K. Shukla, H. Kim, S. Park, M. Min and V. Antonucci, *Appl. Surf. Sci.*, 172 (2001) 1.
28. B.Y. Xia, H.B. Wu, N. Li, Y. Yan, X.W. Lou and X. Wang, *Angew. Chem. Int. Edit.*, 54 (2015) 12.
29. Q. Huang, H. Yang, Y. Tang, T.S. Lu and D.L. Akins, *Electrochem. Commun.*, 8 (2006) 8.
30. Ma.J, Ai. D and Xie X, *Particuology*, 2 (2011)155.
31. Lizcano.Valbuena, William. H, Valdecir. A, Paganin and Ernesto R. Gonzalez, *Electrochim. Acta*, 22 (2002) 3715.
32. Laurent. Brocq. M, Job. N and Eskenazi. D, *Appl. Catal. B-Environ.*, 147(2014) 453.
33. S. Wang, R. Guo, W. Pan, M. Li, P. Sun, S. Liu and S. Liu, *Phys. Chem. Chem. Phys.*, 19 (2017) 5333.
34. D.S. Sholl, J.A. Steckel, Density functional theory: a practical introduction, 2009, Hoboken.